Low-energy electron-impact ionization of argon: Three-dimensional cross section

X. Ren,[1,*] T. Pflüger,[1] J. Ullrich,[1,2] O. Zatsarinny,[3] K. Bartschat,[3] D. H. Madison,[4] and A. Dorn[1]

[1]*Max-Planck-Institut für Kernphysik, Saupfercheckweg 1, 69117 Heidelberg, Germany*

[2]*Physikalisch-Technische Bundesanstalt, Bundesallee 100, 38116 Braunschweig, Germany*

[3]*Department of Physics and Astronomy, Drake University, Des Moines, Iowa 50311, USA*

[4]*Physics Department, Missouri University of Science and Technology, Rolla, Missouri 65409, USA*

(Received 17 January 2012; published 2 March 2012)

Low-energy ($E_0 = 70.8$ eV) electron-impact single ionization of a $3p$ electron in argon has been studied experimentally and theoretically. Our measurements are performed using the so-called reaction microscope technique, which can cover nearly a full 4π solid angle for the emission of a secondary electron with energy below 15 eV and projectile scattering angles ranging from -8° to -30°. The measured cross sections are internormalized across all scattering angles and ejected energies. Several theoretical models were employed to predict the triple-differential cross sections (TDCSs). They include a standard distorted-wave Born approximation (DWBA), a modified version to account for the effects of postcollision interaction (DWBA-PCI), a hybrid second-order distorted-wave plus R-matrix (DWB2-RM) method, and the recently developed B-spline R-matrix with pseudostates (BSR) approach. The relative angular dependence of the BSR cross sections is generally found to be in reasonable agreement with experiment, and the importance of the PCI effect is clearly visible in this low-energy electron-impact ionization process. However, there remain significant differences in the magnitude of the calculated and the measured TDCSs.

DOI: 10.1103/PhysRevA.85.032702 PACS number(s): 34.80.Dp

I. INTRODUCTION

Electron-impact ionization is a fundamental process in atomic physics. Its detailed understanding is of significant importance in many fields of science and technology, such as astrophysics, the physics of the upper atmosphere, plasmas, and radiation physics. Kinematically complete experiments, so-called $(e,2e)$ studies, determine the momentum vectors of all continuum particles, thereby serving as a powerful tool to test few-body quantum mechanical theories. Such complete $(e,2e)$ experiments have been carried out for more than four decades, covering a broad range of target systems and collision kinematics. The most frequently studied experimental setup is the coplanar scattering geometry, where both final-state electrons are emitted in a common plane that also contains the incoming projectile direction.

In recent years, theory has made tremendous progress in describing the electron-impact ionization process of light quasi-one- and quasi-two-electron atoms. For example, the problem of electron scattering from atomic hydrogen has been solved numerically with fully nonperturbative approaches, such as exterior complex scaling (ECS) [1], convergent close-coupling (CCC) [2], and time-dependent close-coupling (TDCC) [3]. The CCC and TDCC methods have also been successfully extended to describe the electron scattering from helium (see, for example, [4–6] and references therein), provided the residual ion remains in the ground state and hence one electron can effectively be described as a spectator. Recently, a fully nonperturbative treatment based on the B-spline R-matrix with pseudostates (BSR) method, another convergent close-coupling-type approach, has been developed. Excellent agreement with experiment was obtained for electron-impact ionization without excitation and the highly correlated and hence very challenging process of ionization with excitation of helium [7].

For heavier targets, on the other hand, theory is being greatly challenged when it comes to treating electron-impact ionization of a many-electron target with an acceptable degree of accuracy, in particular when a subshell with nonzero orbital angular momentum is ionized (see, for example, [8,9]). Ar $(3p)$ ionization, the topic of this paper, is such a problem. While the momentum-space CCC method was recently applied to calculate ionization of Ne $(2s)$ [8,10], it is not yet applicable to ionization of a p electron in heavier targets such as Ne $(2p)$ or Ar $(3p)$.

Until very recently, when the BSR predictions [11] were tested against our previous experiment [9], all theoretical descriptions of electron-impact ionization of argon treated at least some part of the problem perturbatively. These are based upon the distorted-wave Born approximation (DWBA) [12–16] for both the projectile and the ejected electron, or a hybrid approach where the scattering of the (slow) ejected electron with the residual ion is treated via a close-coupling expansion while the projectile-target interaction is again treated perturbatively up to second order [17]. Some of the models also attempt to account for the final-state postcollision interaction, either through an asymptotically correct wave function in the matrix elements [14], or, much simpler, via the so-called Gamow factor [16,18].

For high- and intermediate-energy electron impact, agreement between experiment and theory is generally good regarding the relative angular dependence (i.e., the shape) of the cross sections in the coplanar geometry; see, e.g., [15–17]. On the other hand, puzzling discrepancies remain in particular outside the scattering plane [9,19]. For low-energy electron-impact ionization, significant differences between experiment and theoretical predictions were observed even inside the scattering plane [20,21]. Outside the scattering plane, only a few experiments for low-energy electron collisions with heavier

*ren@mpi-hd.mpg.de

targets were carried out for equal energy sharing conditions and both final-state electrons being emitted perpendicular to the incident beam [22–24].

Recently, three-dimensional (3D) cross sections for Ar $(3p)$ single ionization by 195 eV electron impact [9,19] were obtained and compared with the hybrid distorted-wave plus R-matrix method. While rather good agreement in the relative shape of the cross sections was observed in the coplanar scattering geometry, significant discrepancies were found perpendicular to the scattering plane. This was attributed to higher-order projectile-target scattering and final-state electron-electron interaction effects [often called postcollision interaction (PCI)]. Furthermore, the drop of the cross-section magnitude in going from small to large projectile scattering angles was stronger in theory than in experiment. Since the physical effects of PCI, the projectile-target interaction, as well as electron exchange and polarization effects should become more pronounced with decreasing projectile energy, the 3D measurements reported here for low-energy electron-impact ionization of argon are expected to provide important benchmark data to test the validity of current and future theories.

In the present work, single ionization of Ar $(3p)$ was measured for 70.8 eV electron impact. The 3D cross sections for projectile scattering angles ranging from $\theta_1 = -8^\circ$ to -30° and ejected electron energies E_2 from 3 to 15 eV are presented together with cuts in the scattering and one perpendicular plane. The experimental data are compared with theoretical predictions from several calculations based on the standard DWBA approach, DWBA plus PCI, and the hybrid second-order distorted-wave Born plus R-matrix (close-coupling) approach (DWB2-RM). Furthermore, the fully nonperturbative BSR approach was employed. The absolute scale of the experimental data was not determined independently. Instead, the relative data were visually normalized to the BSR predictions to give good fits at $\theta_1 = -8^\circ$ and $E_2 = 3$ eV. At this angle and energy (and also for $E_2 = 5$ eV), the shape agreement between experiment and the BSR theory is good both in the scattering plane and the perpendicular plane, as shown in panels (a) and (b) of Figs. 4 and 5 below. It should be noted that all data in the present experiment were recorded simultaneously. Consequently, once the normalization factor has been fixed for one case, the cross sections for all kinematic geometries are internormalized across all recorded scattering angles and all ejected electron energies.

II. EXPERIMENT

The present experiment was performed using an advanced reaction microscope that was particularly designed for electron- and positron-impact experiments [25]. Details of the experimental setup and the procedure were described elsewhere [19,26]. Briefly, a well-focused (1 mm), pulsed electron beam (pulse length $\approx$1.5 ns, repetition rate 180 kHz, $\approx 10^4$ electrons/pulse), generated by a standard thermocathode gun, crosses an argon gas jet (1 mm diameter, 10^{12} atoms/cm^3), which is produced in a three-stage supersonic gas expansion. Using uniform electric and magnetic fields, the fragments in the final state are projected onto two position- and time-sensitive multihit detectors equipped with fast delay-line readout. For single ionization a triple coincidence of both outgoing electrons (e_1 and e_2) and the recoil ion is recorded. From the positions of the hits and the times of flight (TOF), the vector momenta of the detected particles can be calculated. Note that the projectile beam axis (defining the longitudinal direction) is adjusted exactly parallel to the electric and magnetic extraction fields. Therefore, after passing the target gas jet, the beam arrives at the center of the electron detector, where a central bore in the multichannel plates allows for the undeflected electrons to pass without inducing a hit. In this way, a large part of the full solid angle is covered while there are acceptance holes for electron emission under small forward and backward angles. The cross sections presented here cover the full azimuthal angular range and polar angular ranges of $30^\circ \leqslant \theta_2 \leqslant 150^\circ$ for $E_2 = 3$ eV, $30^\circ \leqslant \theta_2 \leqslant 160^\circ$ for $E_2 = 5$ eV, and $40^\circ \leqslant \theta_2 \leqslant 170^\circ$ for $E_2 = 15$ eV. The momentum resolution for the detected electrons is about 0.05 a.u. This translates into angular resolutions of $\Delta\theta = 5^\circ$ for a slow final-state electron with 5 eV kinetic energy and $\Delta\theta = 2^\circ$ for the forward-scattered projectile electron with about 50 eV energy.

III. THEORETICAL APPROACHES

A. DWBA and DWBA-PCI

The DWBA approach has been presented in several previous publications [14,15], so only a brief description will be presented here. The distorting potential contains three components, $U_i = U_s + U_E + U_{CP}$, where U_s includes the nuclear contribution plus a spherically symmetric approximation for the interaction between the projectile electron and the target electrons, which is obtained from the quantum mechanical charge density of the target. Furthermore, U_E is the exchange potential of Furness and McCarthy [27], which approximates the effect of the continuum electron exchanging with the passive bound electrons in the atom, and U_{CP} is the correlation-polarization potential of Perdew and Zunger [28].

Prideaux and Madison [14,15] included the final-state Coulomb interaction between the scattered and ejected electrons (PCI) directly in the approximation for the final-state wave function. They called this approximation the three-body distorted-wave (3DW) approach. One of the important benefits of this approach lies in the fact that any physical effect included in the final-state wave function is automatically included to all orders of perturbation theory. One of the disadvantages of this approach lies in the fact that a full six-dimensional (6D) integral is required for the T-matrix. Due to the numerical difficulties associated with evaluating 6D integrals, several approximations have been proposed to simplify the integral. The Coulomb interaction between the two electrons can be expressed as a product of the Gamow factor and a ${}_1F_1$ hypergeometric function, and it is this function that causes the problem. Botero and Macek [29] (see also Whelan *et al.* [30]) proposed neglecting the hypergeometric function and just using the Gamow factor. With this approximation, the electron-electron repulsion factors out of the integral, and the net effect is to multiply the DWBA amplitude by the Gamow factor. Kheifets *et al.* [16] recently showed that approximating the Coulomb interaction by the Gamow factor significantly improved agreement between experiment and

theory for high-energy ionization of inert gases, particularly at larger scattering angles. Ward and Macek [18] proposed a low-energy approximation, keeping the hypergeometric function but evaluating it for an average separation between the electrons. Al-Hagan *et al*. [31] recently found that this was a good approximation for low-energy ionization of molecular hydrogen. We performed some test calculations using the full 3DW approximation, which indicated that PCI was too strong in the 3DW approach. This observation is consistent with Jones *et al*. [32] who argued that the full strength Coulomb interaction between the two continuum electrons may be too strong for small separations. Consequently, we use the Ward-Macek approximation to account for PCI in the present work.

B. DWB2-RM

As mentioned above, a partially successful theory for electron-impact ionization has been a hybrid approach, in which the interaction of a "fast" projectile electron with the target is described by a first-order or second-order distorted-wave approach, while the initial bound state and the scattering of a "slow" ejected electron from the residual ion is treated by an R-matrix (RM) approach. These DWB1-RM [33,34] and DWB2-RM [35] models were formulated for highly asymmetric kinematics and small energy losses compared to the incident energy.

Details of the hybrid approach can be found in many previous publications, e.g., [9,17,34] and hence will not be repeated here. Given that emission of the $3p$ electron is generally the dominant ionization process in the kinematical regime considered here, it is not surprising that using either a first-order or an approximate second-order treatment of the projectile produced very similar results. Also, coupling only the two final ionic states $(3s^2 3p^5)\,^2P^o$ and $(3s3p^6)\,^2S$, rather than employing a much larger nonrelativistic R-matrix with pseudostates (RMPS) expansion for the ejected-electron–residual-ion problem, was generally found to be sufficient. A key issue, on the other hand, is the description of the initial bound state and the final ionic states included in the close-coupling expansion for the electron scattering from the residual ion. In the hybrid method, we use the multiconfiguration expansions developed by Burke and Taylor [36] for the corresponding photoionization problem.

C. BSR

The BSR method is based upon an entirely different formulation than the previous theories. It basically contains two steps, namely, (i) the treatment of electron collisions with neutral argon using an extensive close-coupling expansion that contains both physical and pseudostates, with the latter being used to approximate the effect of high-lying discrete Rydberg states as well as the coupling to various (depending on the final ionic states) ionization continua, and (ii) the construction of the *ionization* amplitude by combining the scattering amplitudes for *excitation* of the pseudostates using coefficients obtained by direct projection of the wave function to the various scattering channels associated with a particular final ionic state.

For the case at hand, we performed a nonrelativistic R-matrix with pseudostates calculation for e-Ar collisions with a total of 482 states in the close-coupling expansion. The atomic wave functions for neutral Ar were obtained by the B-spline box-based close-coupling method [37]. They were first expanded in terms of products of N-electron ionic states and radial functions for the outer electron. In the present model, we included the $(3s^2 3p^5)\,^2P^o$, $(3s3p^6)\,^2S$, and $(3s^2 3p^4 3d)\,^2S$ states of Ar^+, based on the experienced gained in related work by Guan *et al*. [38].

The radial functions for the outer electron were expanded in a B-spline basis. The expansion coefficients were obtained by diagonalizing the $(N+1)$-electron target Hamiltonian matrix inside a box of radius $a = 28\ a_0$, where $a_0 = 0.529 \times 10^{-10}$ m denotes the Bohr radius. These functions were forced to vanish at the edge of the box. Along with the physical states, this scheme provides a set of pseudostates that, as mentioned above, represent the Rydberg spectrum and the ionization continua. The number of physical bound states and the density of the continuum pseudostates depend upon the radius of the box and the number of B splines. We used 69 B splines of order 8 on a semiexponential grid of knots. This results in 482 physical and pseudotarget states with coupled orbital angular momenta $L = 0$–5 and energies reaching up to 80 eV.

We then obtained the scattering amplitudes for excitation of all pseudostates using our suite of BSR codes [39] for electron collisions. Contributions from $(N+2)$-electron symmetries with coupled orbital angular momenta up to 25 were included in the partial-wave expansion. The present model contained up to 1445 scattering channels, leading to generalized eigenvalue problems with matrix dimensions up to 90 000 in the B-spline basis. The corresponding solutions were obtained with a newly developed parallelized version of the BSR complex.

The last, and most crucial, step in the process is the generation of the ionization amplitudes. This is done by summing up the amplitudes for excitation of all energetically accessible pseudostates, with the expansion factors given by the overlap of the pseudostates and the true continuum functions [7]. At this stage in the calculation, consistency between the models for the bound states (physical and pseudo) and the physical continuum scattering channels is critical. We ensure this consistency by employing the same expansions including the three ionic states $(3s^2 3p^5)\,^2P^o$, $(3s3p^6)\,^2S$, and $(3s^2 3p^4 3d)\,^2S$ states mentioned above.

The key point of the BSR method is the use of B-splines as a universal and effectively complete basis to describe the projectile electron in the close-coupling expansion of the collision system. A distinctive feature of our BSR implementation is the possibility to employ individually optimized, and hence "nonorthogonal" orbitals to describe the target states. Furthermore, we do not restrict the projectile orbitals to be orthogonal to the target orbitals either. Although the lack of these restrictions makes the setting up of the Hamiltonian matrix significantly more complicated than in the standard R-matrix approach [40], the flexibility of the method has proven to be a major advantage on many occasions. Since we can generate accurate descriptions of both the ionic and the neutral states with relatively compact multiconfiguration expansions, the principal purpose of the pseudostates is to approximate the coupling to high-lying Rydberg states and the ionization continua.

IV. RESULTS

Three-dimensional triple-differential cross sections (TDCSs) of Ar ($3p$) ionization as a function of the low-energy electron emission angle θ_2 are presented in Fig. 1 for different projectile scattering angles (θ_1) and ejected electron energies (E_2). As shown in panel (e), the projectile is coming in from the bottom (k_0) and is scattered to the left (k_1). These two vectors define the scattering plane indicated by the dashed frame. In these 3D patterns, the TDCS for a particular direction is given as the distance from the origin of the plot (also corresponding to the collision point) to the point on the surface that is intersected by the ionized electron's emission direction. The experimental 3D cross sections are shown in panels (a), (e), and (i) of Fig. 1. Since their absolute scale was not measured directly, the experimental cross sections were normalized to the BSR calculation at $\theta_1 = -8^\circ$ and $E_2 = 3$ eV [discussed below in Figs. 4(a) and 4(b)]. Thus, at these kinematics, experiment [Fig. 1(a)] and the BSR results [Fig. 1(b)] agree well in magnitude. In these and all following diagrams a 10° angular binning of the experimental data was chosen to obtain sufficient statistical significance of the cross-section values. While this binning can smear out sharp cross-section structures, such features are not predicted by any of the theories in the experimentally accessible angular range.

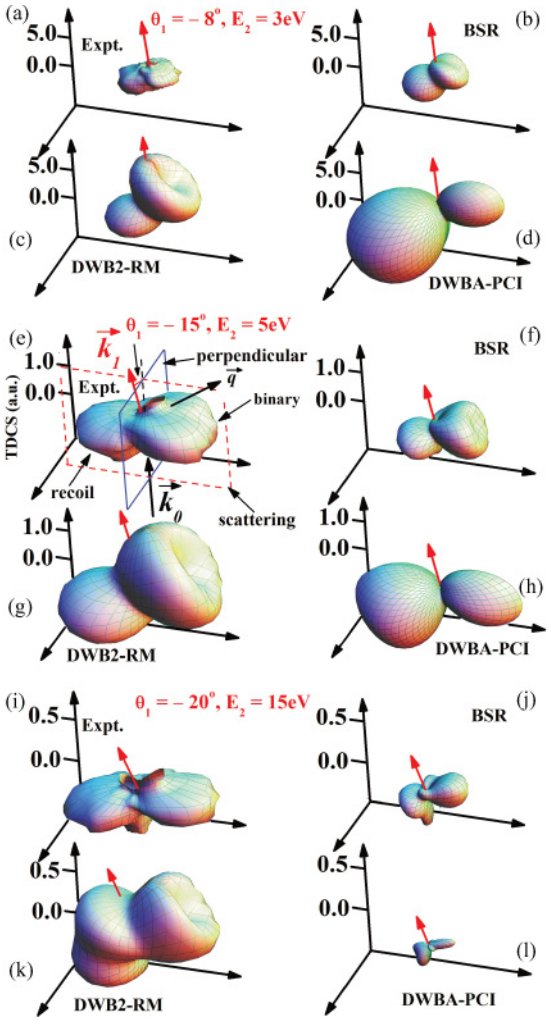

FIG. 1. (Color online) Three-dimensional presentation of the TDCS for single ionization of Ar ($3p$) by 70.8 eV electron impact as a function of the low-energetic (E_2) electron emission angle for selected projectile scattering angles (θ_1) and ejected electron energies (E_2). (a)−(d): $\theta_1 = -8^\circ$ ($\pm 1.5^\circ$) and $E_2 = 3$ eV (± 1.0 eV); (a): experiment, (b) BSR theory, (c) DWB2−RM theory, (d) DWBA-PCI theory. (e)−(h): $\theta_1 = -15^\circ$ ($\pm 2.5^\circ$) and $E_2 = 5$ eV (± 1.5 eV). (i)−(l): $\theta_1 = -20^\circ$ ($\pm 3.0^\circ$) and $E_2 = 15$ eV (± 2.0 eV).

All experimental data exhibit the basic features of binary and recoil lobes. The emitted electron is repelled by the scattered projectile due to the long-range nature of the Coulomb force, thus giving rise to the so-called postcollision interaction. Therefore, the binary and recoil lobes are tilted away from the scattered projectile direction. In addition, the binary lobe exhibits a much flatter shape in comparison with the 3D emission patterns in the high- and intermediate-energy regime [19,41]. Furthermore, the 3D patterns allow for a complete view of the electron emission and reveal more features. For example, significant cross-section values are clearly observed perpendicular to the scattering plane, bridging the angular range between the binary and recoil lobes. Finally, there are new structures, in particular for large projectile scattering angles. At $\theta_1 = -20^\circ$ the experimental pattern shows an additional lobe in the projectile backwards direction and small lobes in the minimum between the binary and the recoil lobes. In panels (e) and (i) of Fig. 1 there is also the indication of increasing cross section in the forward direction. Unfortunately, there is an acceptance hole in the electron detector, which prevents tracing this feature to the forward direction.

Theoretical results are also provided in Fig. 1 with the models of BSR in panels (b), (f), and (j), DWB2-RM in panels (c), (g), and (k), and DWBA-PCI in panels (d), (h), and (l). Note that the PCI effect is not included in the DWB2-RM approach while it is accounted for in the DWBA-PCI model. Clearly, the theoretical predictions differ strongly from each other, reflecting the fact that the theoretical treatment of electron-impact ionization of many-electron targets is very complicated and the results are very sensitive to the details of the model employed.

The BSR theory generally produces good agreement with the experimental 3D cross sections. The DWB2-RM calculations often also yield the relative shape of the experimental 3D cross sections, except that strong discrepancies are observed near the scattered projectile direction. This problem is likely due to the missing PCI effect in this model. The DWBA-PCI calculations exhibit reasonable agreement with the experimental data in the scattering plane but strong discrepancies for the cross sections outside the scattering plane.

A significant issue regarding theory and experiment is the predicted magnitude of the cross sections in comparison with the experimental data. It is clearly seen that the experimental data normalized to the BSR calculation [in Fig. 1(a)] at $\theta_1 = -8^\circ$ and $E_2 = 3$ eV are relatively smaller in magnitude than the theoretical prediction from the DWBA-PCI method in panel (d). The results at $\theta_1 = -20^\circ$ and $E_2 = 15$ eV [Fig. 1(i)] indicate that the experimental magnitude of the cross section is smaller than the DWB2-RM prediction in panel (k), but larger

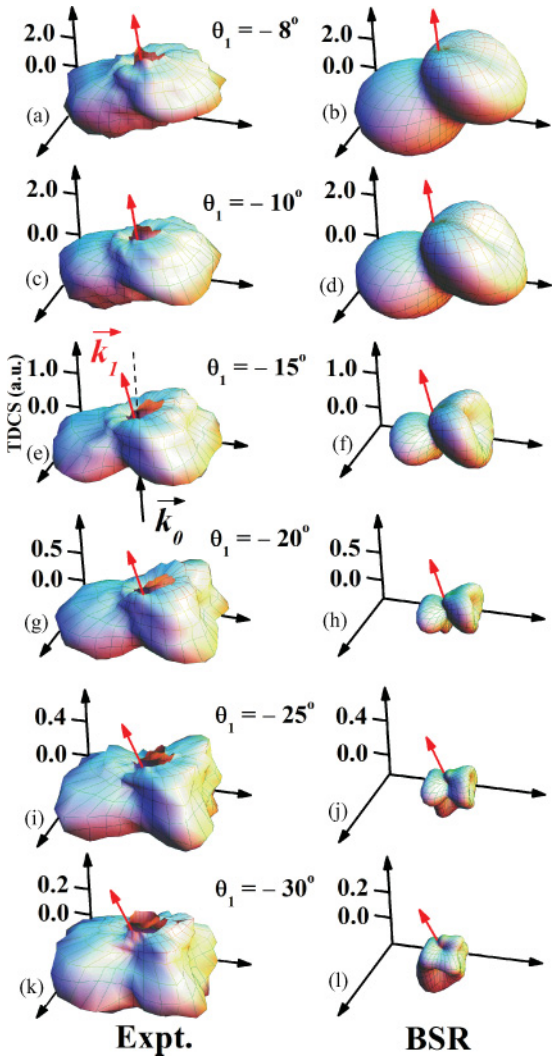

FIG. 2. (Color online) Three-dimensional presentation of the TDCS for single ionization of Ar ($3p$) by 70.8 eV electron impact as a function of the emission angle of an electron with kinetic energy $E_2 = 3$ eV (± 1.0 eV) and different projectile scattering angles (θ_1). (a) and (b): $\theta_1 = -8°(\pm 1.5°)$; (c) and (d): $\theta_1 = -10°$ ($\pm 2.0°$); (e) and (f): $\theta_1 = -15°$ ($\pm 2.5°$); (g) and (h): $\theta_1 = -20°$ ($\pm 3.0°$); (i) and (j): $\theta_1 = -25°$ ($\pm 3.0°$); (k) and (l) $\theta_1 = -30°$ ($\pm 3.5°$). Left column: experiment. Right column: BSR theory.

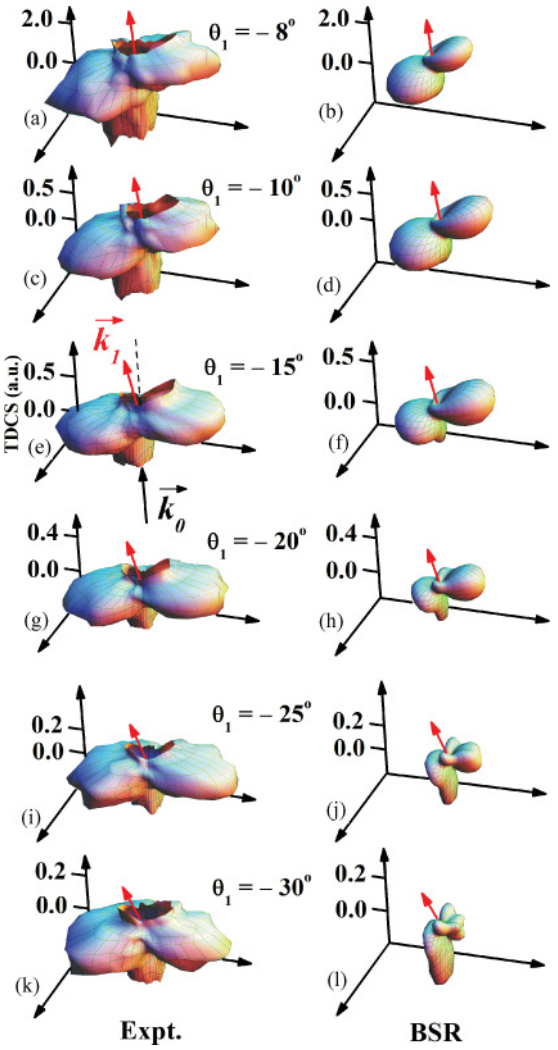

FIG. 3. (Color online) Same as Fig. 2 but for $E_2 = 15$ eV (± 2.0 eV).

than the BSR prediction in panel (j) and the DWBA-PCI result panel (l)].

The experimental 3D cross sections for projectile scattering angles from $\theta_1 = -8°$ to $-30°$ are presented in Figs. 2 and 3 for ejected electron energies of $E_2 = 3$ and 15 eV, respectively, in comparison with the BSR predictions. Concerning the overall shape of the 3D TDCSs, there is good agreement for $E_2 = 3$ eV. However, the most significant issue is the predicted magnitude of the cross sections in comparison with the experiment. One can clearly see from Figs. 2 and 3 that the magnitude of the experimental cross section decreases when changing the scattering angle from $\theta_1 = -8°$ to $-30°$. This decrease also occurs in the theoretical predictions, but the calculated decrease in magnitude is much more rapid than what is seen in the experimental data. This phenomenon is similar to that observed in the single ionization of Ar ($3p$) by 195 eV electron impact in [9]. At this point we cannot rule out the possibility that the discrepancy may partially be caused by the experimental resolution. Unfortunately, it is impractical to perform all the necessary additional calculations to convolute the theoretical predictions with the detector function. A detailed discussion of potential issues for the 195 eV case is provided in [11].

For a more quantitative comparison between experiment and theory, cuts through the 3D images of the TDCS are exhibited in Fig. 4. The cross sections in the scattering plane and the perpendicular planes [as indicated by the dashed and solid frames in Fig. 1(e)] are presented in the left and right columns of Fig. 4, respectively, as a function of the ejected electron ($E_2 = 3$ eV) emission angle θ_2 for projectile scattering angles from $\theta_1 = -8°$ to $-30°$. The data are integrated over an out-of-plane angular range of $\pm 10°$. This should have only minor implications for the scattering plane where the cross section changes slowly for small out-of-plane angles. In contrast, for the perpendicular plane some of the theoretical results show sharp minima in between the binary and recoil lobes at $\theta_2 = 90°$ and 270°. These could be partly filled up in the experimental curves. Also included in Fig. 4

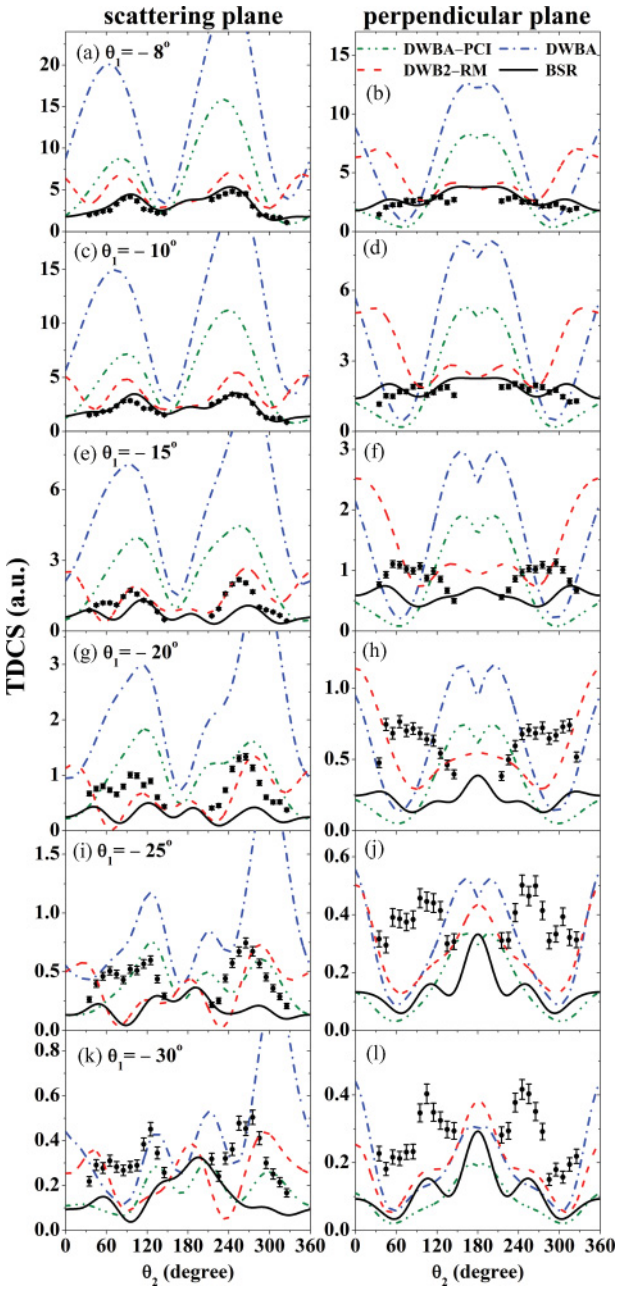

FIG. 4. (Color online) TDCS Ar ($3p$) as a function of the emission angle of an electron with kinetic energy $E_2 = 3$ eV (± 1.0 eV). The other electron's detection angle is: (a) and (b) $\theta_1 = -8°(\pm 1.5°)$; (c) and (d) $\theta_1 = -10°(\pm 2.0°)$; (e) and (f) $\theta_1 = -15°(\pm 2.5°)$; (g) and (h) $\theta_1 = -20°(\pm 3.0°)$; (i) and (j) $\theta_1 = -25°(\pm 3.0°)$; (k) and (l) $\theta_1 = -30°(\pm 3.5°)$. The experimental data are compared with theoretical predictions from the DWBA, DWBA-PCI, DWB2-RM, and BSR approaches. Left column: TDCS in the scattering plane. Right column: TDCS in the perpendicular plane.

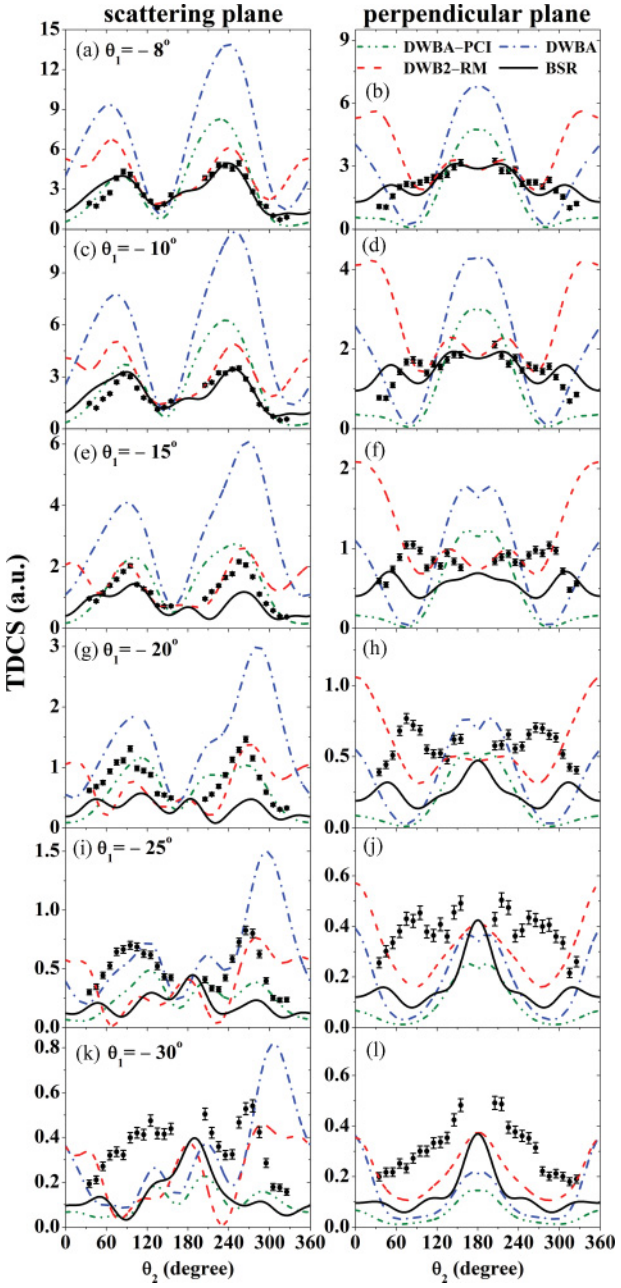

FIG. 5. (Color online) Same as Fig. 4 but for $E_2 = 5$ eV (± 1.5 eV).

are the theoretical predictions from the DWBA, DWBA-PCI, DWB2-RM, and BSR models. Regarding the relative angular dependence of the TDCSs, the calculations for the coplanar geometry are generally in reasonable agreement with the experimental data. As illustrated by the left column of Fig. 4, the BSR calculations reproduce rather well the relative shapes of the experimental TDCSs for small projectile scattering angles. At larger projectile scattering angles, more significant differences arise, such as small variances of the peak positions at 270° or an overestimate of the 180° peak in the BSR theory. The DWB2-RM model also predicts the general shape of the measured TDCSs, except that strong discrepancies are observed in the angular range of θ_2 close to 0° and 360° due to the neglected PCI effect. Between DWBA and DWBA-PCI, the latter clearly resembles the data better, especially for the larger projectile scattering angles. At $\theta_1 = -20°$ in panel (g), $\theta_1 = -25°$ in panel (i), and $\theta_1 = -30°$ in panel (k), even the relative shape of the experimental TDCSs is not well reproduced by the DWBA calculations. These findings highlight the importance of the PCI effect in the low-energy electron-impact ionization process.

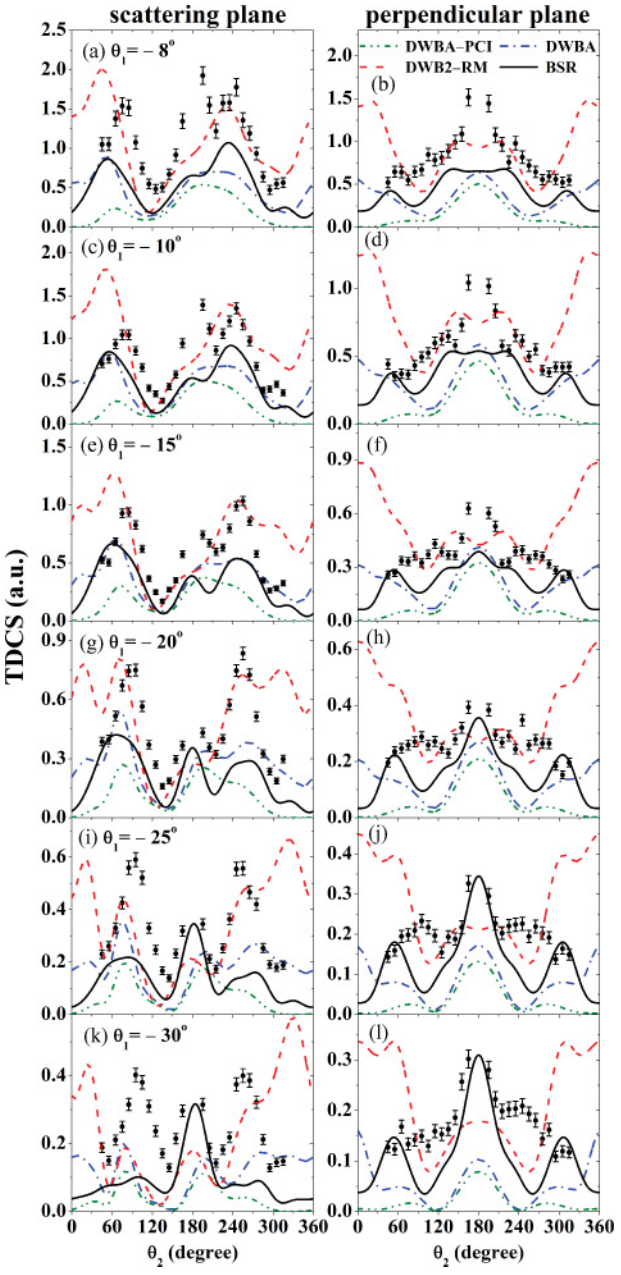

FIG. 6. (Color online) Same as Fig. 4 but for $E_2 = 15$ eV (± 2.0 eV).

In the perpendicular plane, significant discrepancies are observed between experiment and the theoretical predictions based on the DWBA, DWBA-PCI, and DWB2-RM approaches. The DWB2-RM model predicts much higher intensities of the cross section in the angular range of θ_2 close to 0° and 360° than experiment, which is again likely due to the neglect of PCI in the model. The DWBA results differ from the experimental data when θ_2 is close to 0° or 180°. The DWBA-PCI calculation provides an improvement over the direct DWBA calculations in that its predictions become reasonable in the angular range of θ_2 close to 0° and 360°. This indicates once again that the PCI effect plays a very important role in the low-energy ionization processes. The BSR theory, while reproducing the relative shape of the measured TDCSs much better than the other theories, still misses some features at higher scattering angles.

As expected from Figs. 1–3, the most notable difference between theory and experiment in Fig. 4 concerns the magnitude of the cross sections. The predicted magnitude from the DWBA model is a factor of 5 higher than the BSR calculation for the scattering angle of $\theta_1 = -8°$, as seen in Figs. 4(a) and 4(b). At $\theta_1 = -30°$ displayed in panels (k) and (l), however, the normalized measured peak magnitudes of the TDCS are a factor of 2–3 larger than all calculations. As mentioned previously, the cause of this issue is unknown at the present time. It might indicate that the theoretical models need to be further improved to accurately describe the physics of low-energy electron-impact ionization of many-electron systems [9]. On the other hand, further experiments are also required to confirm the present observations. In particular, it would be desirable to test the apparently very strong dependence of the TDCS on the projectile detection angle in the coplanar geometry by a conventional $(e,2e)$ apparatus.

TDCSs for ejected electron energies of $E_2 = 5$ and 15 eV are presented in Figs. 5 and 6, respectively, for projectile scattering angles from $\theta_1 = -8°$ to $-30°$. Also included in the figures are the results from the BSR, DWB2-RM, DWBA, and DWBA-PCI models. It is found once again that the relative angular dependence of the large cross sections in both the scattering plane and perpendicular plane is well reproduced by the BSR theory. Concerning the dominant features of the TDCSs, the DWBA-PCI model provides a better description of the relative shape of the cross sections, especially for the larger scattering angles (as seen in Figs. 5 and 6 for $\theta_1 = -20°$, $-25°$, and $-30°$) than the DWBA and DWB2-RM methods that neglect the PCI effect. Not surprisingly, the most significant issue between experiment and theory remains the magnitude of the cross sections. The differences reach up to a factor of 2–3 for the kinematic condition of $\theta_1 = -30°$, as shown in the bottom row of Figs. 5 and 6.

V. CONCLUSIONS

A comprehensive investigation of electron-impact ionization of Ar $(3p)$ has been reported for 70.8 eV projectile energy. The three-dimensional triple-differential cross sections obtained experimentally were internormalized across all scattering angles (θ_1 from $-8°$ to $-30°$) and ejected energies (E_2 from 3 to 15 eV). The experimental data were compared with predictions from DWBA, DWBA-PCI, DWB2-RM, and BSR models. The relative angular dependence of the cross sections calculated with the nonperturbative BSR method is generally in best agreement with experiment for the 3D emission pattern, as well as for selected cuts through the scattering and perpendicular planes. The importance of PCI effects in low-energy electron-impact ionization was clearly identified by comparisons between experiment and the various theoretical predictions.

The remaining differences between our experimental data and the theoretical predictions occur in very challenging energy and angle regimes, usually where the cross sections are small. Consequently, it is difficult to draw unambiguous conclusions regarding the origins for these discrepancies.

Further studies, experimental and theoretical, seem highly desirable to confirm the present observations.

ACKNOWLEDGMENTS

This work was supported by the Deutsche Forschungsgemeinschaft (DFG) under Project No. RE 2966/1-1 (X.R.) and by the United States National Science Foundation under Grants No. PHY-1068237 (D.H.M.), No. PHY-0903818 (O.Z. and K.B.), and No. PHY-1068140 (K.B.). Additional support from Drake University through a Troyer Research Fellowship (K.B.) is also gratefully acknowledged.

[1] T. N. Resigno, M. Baertschy, W. A. Isaacs, and C. W. McCurdy, Science **286**, 2474 (1999).
[2] I. Bray, Phys. Rev. Lett. **89**, 273201 (2002).
[3] J. Colgan and M. S. Pindzola, Phys. Rev. A **74**, 012713 (2006).
[4] J. Colgan, M. Foster, M. S. Pindzola, I. Bray, A. T. Stelbovics, and D. V. Fursa, J. Phys. B **42**, 145002 (2009).
[5] I. Bray, D. V. Fursa, A. S. Kadyrov, and A. T. Stelbovics, Phys. Rev. A **81**, 062704 (2010).
[6] X. Ren, I. Bray, D. V. Fursa, J. Colgan, M. S. Pindzola, T. Pflüger, A. Senftleben, S. Xu, A. Dorn, and J. Ullrich, Phys. Rev. A **83**, 052711 (2011).
[7] O. Zatsarinny and K. Bartschat, Phys. Rev. Lett. **107**, 023203 (2011).
[8] L. R. Hargreaves, M. A. Stevenson, and B. Lohmann, J. Phys. B **43**, 205202 (2010).
[9] X. Ren, A. Senftleben, T. Pflüger, A. Dorn, K. Bartschat, and J. Ullrich, Phys. Rev. A **83**, 052714 (2011).
[10] A. Naja, E. M. Staicu Casagrande, A. Lahmam-Bennani, M. Stevenson, B. Lohmann, C. Dal Cappello, K. Bartschat, A. Kheifets, I. Bray, and D. V. Fursa, J. Phys. B **41**, 085205 (2008).
[11] O. Zatsarinny and K. Bartschat, Phys. Rev. A **85**, in press (2012).
[12] I. E. McCarthy, Z. Phys. D **23**, 287 (1992).
[13] X. Zhang, C. T. Whelan, and H. R. J. Walters, Z. Phys. D **23**, 301 (1992).
[14] A. Prideaux and D. H. Madison, Phys. Rev. A **67**, 052710 (2003).
[15] A. Prideaux, D. H. Madison, and K. Bartschat, Phys. Rev. A **72**, 032702 (2005).
[16] A. S. Kheifets, A. Naja, E. M. Staicu Casagrande, and A. Lahmam-Bennani, J. Phys. B **41**, 145201 (2008).
[17] K. Bartschat and O. Vorov, Phys. Rev. A **72**, 022728 (2005).
[18] S. J. Ward and J. H. Macek, Phys. Rev. A **49**, 1049 (1994).
[19] X. Ren, A. Senftleben, T. Pflüger, A. Dorn, K. Bartschat, and J. Ullrich, J. Phys. B **43**, 035202 (2010).
[20] K. D. Winkler, D. H. Madison, and H. P. Saha, J. Phys. B **32**, 4617 (1999).
[21] B. Rouvellou, S. Rioual, J. Röder, A. Pochat, J. Rasch, C. T. Whelan, H. R. J. Walters, and R. J. Allan, Phys. Rev. A **57**, 3621 (1998).
[22] A. J. Murray, N. J. Bowring, and F. H. Read, J. Phys. B **33**, 2859 (2000).
[23] J. F. Williams, R. W. van Boeyen, and S. Samarin, Phys. Rev. A **71**, 052709 (2005).
[24] K. L. Nixon, A. J. Murray, and C. Kaiser, J. Phys. B **43**, 085202 (2010).
[25] J. Ullrich, R. Moshammer, A. Dorn, R. Dörner, L. Ph. H. Schmidt, and H. Schmidt-Böcking, Rep. Prog. Phys. **66**, 1463 (2003).
[26] M. Dürr, C. Dimopoulou, A. Dorn, B. Najjari, I. Bray, D. V. Fursa, Z. Chen, D. H. Madison, K. Bartschat, and J. Ullrich, J. Phys. B **39**, 4097 (2006).
[27] J. B. Furness and I. E. McCarthy, J. Phys. B **6**, 2280 (1973).
[28] J. P. Perdew and A. Zunger, Phys. Rev. B **23**, 5048 (1981).
[29] J. Botero and J. H. Macek, Phys. Rev. Lett. **68**, 576 (1992).
[30] C. T. Whelan, R. J. Allan, and H. R. J. Walters, J. Phys. IV **3**, 39 (1993).
[31] O. Al-Hagan, C. Kaiser, D. H. Madison, and A. J. Murray, Nat. Phys. **5**, 59 (2009).
[32] S. Jones, D. H. Madison, A. Franz, and P. L. Altick, Phys. Rev. A **48**, R22 (1993).
[33] K. Bartschat and P. G. Burke, J. Phys. B **20**, 3191 (1987).
[34] K. Bartschat and P. G. Burke, J. Phys. B **21**, 2969 (1988).
[35] R. H. G. Reid, K. Bartschat, and A. Raeker, J. Phys. B **31**, 563 (1998); corrigendum: J. Phys. B **33**, 5261 (2000).
[36] P. G. Burke and K. T. Taylor, J. Phys. B **8**, 2620 (1975).
[37] O. Zatsarinny and C. Froese Fischer, J. Phys. B **35**, 4669 (2002).
[38] X. Guan, C. J. Noble, O. Zatsarinny, K. Bartschat, and B. I. Schneider, Phys. Rev. A **78**, 053402 (2008).
[39] O. Zatsarinny, Comput. Phys. Commun. **174**, 273 (2006).
[40] P. G. Burke, *R-Matrix of Atomic Collisions: Application to Atomic, Molecular, and Optical Processes* (Springer, New York, 2011).
[41] M. Dürr, C. Dimopoulou, B. Najjari, A. Dorn, K. Bartschat, I. Bray, D. V. Fursa, Z. Chen, D. H. Madison, and J. Ullrich, Phys. Rev. A **77**, 032717 (2008).